Proceedings of the ASME 2010 3rd Joint US-European Fluids Engineering Summer Meeting and 8th International Conference on Nanochannels, Microchannels, and Minichannels
FEDSM-ICNMM2010
August 1-5, 2010, Montreal, Canada

FEDSM-ICNMM2010-30886

DIRECT NUMERICAL SIMULATION OF TURBULENT FLOWS IN ROUGH PIPES USING AN IMMERSED BOUNDARY METHOD WITH A SPECTRAL REPRESENTATION OF THE ROUGHNESS TOPOGRAPHY

A.T. van Nimwegen and L.M. Portela

Kramers Laboratory
Department of Multi Scale Physics
Delft University of Technology
Prins Bernhardlaan 6, 2628 BW Delft
The Netherlands

L.Portela@tudelft.nl

ABSTRACT

An immersed boundary method, similar to the one used by Kim et al. [1] was developed to implement a varying wall topography into an existing DNS code for pipe flow. Validation using a semi-analytical solution and numerical results showed that the method yields accurate results for laminar flow. Four simulations for turbulent flow where performed, each with a different wall geometry. Wall topographies varying in the axial direction and topographies varying in the azimuthal direction have been considered. Time-averaged as well as instantaneous results are presented for the different geometries. The results for turbulent flow are consistent with the expected physical behaviour. They confirm the hypothesis that flow in the outer layer is largely unaffected by the wall topography.

NOMENCLATURE

D Diameter of the entire computational domain, consisting of the pipe and the immersed boundary.
U Indicates a generic velocity component (can be in any direction).
$\overrightarrow{U}$ Velocity vector.
p Pressure.
r Radial coordinate.
u Radial velocity component
v Angular velocity component
w Axial velocity component
z Axial coordinate
θ Azimuthal coordinate
ν Kinematic viscosity
ρ Fluid density
ϕ Pressure correction
DNS Direct numerical simulation
LES Large eddy simulation
rms root-mean-square

INTRODUCTION

Turbulent flow with rough walls are important in many situations, in particular in industrial pipe flow. Many experimental results have been obtained for rough walls, resulting in a large amount of empirical data. A good example is the Moody diagram [2], which contains the friction at the wall at different Reynolds numbers for different roughness heights. This data is used to make an empirical model for the influence of the roughness on the flow used in engineering simulations. However, the

only information of the roughness incorporated into such an empirical model is the roughness height. More recently, LES/DNS simulations have been done for turbulent flow bounded by roughness with a regular topography (e.g. sinusoidal walls, a regular array of transverse bars or egg carton shape [3–5]). These simulations have shown that the flow near the wall in the inner layer of the pipe is dramatically affected by the topography of the roughness. However, there is no consensus about the influence of the roughness on the flow near the centre of the pipe. Traditionally, it is assumed that the flow in the outer layer is not affected by the roughness and has the same properties as the flow over a smooth wall, albeit with a lower Reynolds number for the same pressure gradient. This is also known as Townsends Reynolds hypothesis [6]. However, some results found in the literature (for instance [7, 8]) challenge this answer [4].

To be able to investigate the influence of the roughness in both the inner and the outer layer of turbulent pipe flow, a tool was developed with which the flow can be studied numerically in great detail. Using this tool pipe flow with arbitrary wall topography can be studied: i.e. not only rough pipes, but also pipes with much more dramatic variations in diameter can be studied. The distance from the centre of the pipe to the wall is a function of both the angular and the axial coordinate, allowing for a broad range of wall topographies to be examined. To this end an existing DNS code for turbulent pipe flow developed by Eggels [9] was extended with an immersed boundary method to include the rough boundary. This code uses a fractional step method to solve the flow, where an FFT-solver is used to solve the Poisson equation for the pressure. Note that this means that the flow, and therefore the wall topography, must be periodic in both the angular and axial direction. In this paper the implementation of this immersed boundary method is discussed, followed by a validation for laminar flow, using both a semi-analytical solution and results from an axisymmetric simulation of laminar flow in a converging-diverging pipe. A further section is devoted to the evaluation of the results for turbulent flow, where numerical issues are addressed and the influence of the grid resolution on the statistics of the flow is discussed. Finally, the results for turbulent flow in several roughness topologies is presented in detail. Attention will be given to both time-averaged and instantaneous quantities.

MODELLING OF THE ROUGH BOUNDARY USING AN IMMERSED BOUNDARY METHOD

This work concerns incompressible flow in a three dimensional domain (a pipe with a rough wall). The governing equations for this type of flow are:

$$\nabla \cdot \overrightarrow{U} = 0 \tag{1}$$

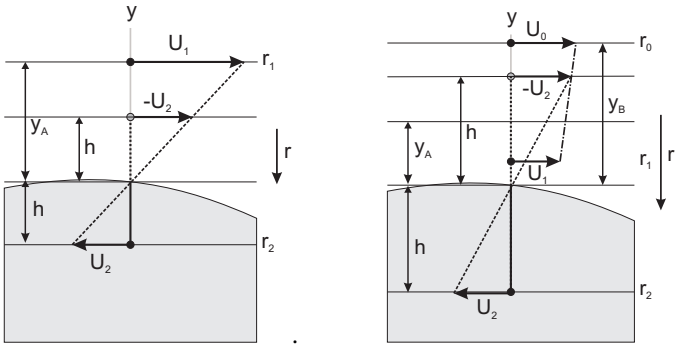

(a) Normal linear interpolation (b) Adjusted linear interpolation

FIGURE 1. LINEAR INTERPOLATIONS: THE BLACK DOTS ARE GRIDPOINTS WHERE THE VELOCITY IS SPECIFIED, THE GRAY DOTS ARE GHOSTPOINTS USED IN THE INTERPOLATION SCHEME

$$\frac{\partial \overrightarrow{U}}{\partial t} + \overrightarrow{U} \cdot \nabla \overrightarrow{U} = -\frac{1}{\rho} \nabla p + \nu \nabla^2 \overrightarrow{U} \tag{2}$$

where $\overrightarrow{U}$ is the fluid velocity, which consists of a radial component u, an angular component v and an axial component w. These equations are solved in the entire domain, in this case a pipe. To this end the equation is discretised and solved on a computational grid. However, when the topography of the domain-wall becomes complex, grid generation of a body-conformal grid will become difficult and fast solvers can no longer be used. The immersed boundary method is a technique to solve flows in complex geometries, while keeping the fast solvers and the regular computational grid. When a fluid flows over a boundary, a force is exerted by the fluid on the wall. This force consists of a shear force parallel to the wall and a pressure force perpendicular to the wall. Applying Newton's third law, it can also be stated that a boundary exerts certain shear and pressure forces on the fluid. By introducing the correct force into the Navier-Stokes equations, the fluid will act as if it flows past a boundary [10]. This is the essence of the immersed boundary method. The force $\overrightarrow{f}$ is represented in the following equation:

$$\frac{\vec{u}^{n+1} - \vec{u}^{n}}{\Delta t} + \mathbf{A}_h(\vec{u}^{n}) = -\frac{1}{\rho} \nabla_h p + \nu \mathbf{D}_h(\vec{u}^{n}) + \mathbf{f}_b^{n+1} \tag{3}$$

This is the discretised Navier-Stokes equation [11], where $\mathbf{A}_h$ is the discretised advection term, $\mathbf{D}_h$ is the discretised diffusion term and $\mathbf{f}_b^{n+1}$ is the discretised force. The superscripts n and $n+1$ indicate the time step. The force in this equation can be used to adjust the velocity $\vec{u}^{n+1}$ in the next timestep. If the value

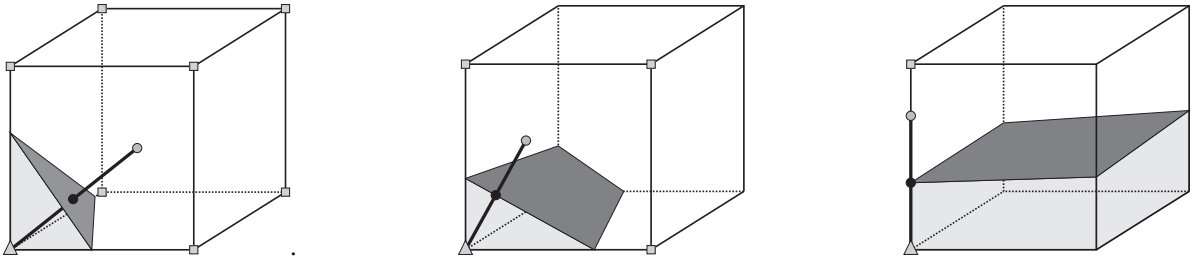

(a) Trilinear interpolation (b) Bilinear interpolation (c) Linear interpolation

FIGURE 2. DIFFERENT TYPES OF INTERPOLATION

of $\vec{u}^{n+1}$ is known, the force is given by:

$$\mathbf{f}_b^{n+1} = \frac{\vec{u}^{n+1} - \vec{u}^n}{\Delta t} + \mathbf{A}_h(\vec{u}^n) + \frac{1}{\rho}\nabla_h p - \nu \mathbf{D}_h(\vec{u}^n) \tag{4}$$

The velocity $\vec{u}^{n+1}$ is found using interpolations. A simple example of such an interpolation is given in figure 1(a). On the wall a no-slip condition is assumed. Velocity U_2 should be set in such a way that the velocity at the immersed boundary is equal to zero. This is done using the following formula:

$$U_2 = -\frac{h}{y_A} U_1 \tag{5}$$

where U_1 is the velocity outside the boundary, which is already solved for the current timestep. This is only a simple linear interpolation, but in the method implemented in this paper more complicated interpolations using multiple velocities outside the wall are also used, to increase the accuracy of the method. These interpolations are discussed in more detail in the coming subsection. Note that the interpolation of the velocities follows the predictor step. In the predictor step only the average pressure gradient $\overline{\nabla p}$, constant throughout the pipe, is considered. The corrector step is used to find $\nabla\phi$ such that:

$$\nabla p = \overline{\nabla p} + \nabla\phi \tag{6}$$

$\nabla\phi$ is an adjustment of the pressure to satisfy continuity. This adjustment changes the velocity field, possibly leading to an in- or outflow through the wall. In order to repair this, mass sources are used. These will be explained in a different subsection. Note that each time-step gives rise to only a small correction in the velocity field. The correction due to the pressure correction is even smaller, thus making it unnecessary to incorporate the pressure fluctuations of the previous timestep into the predictor step of the current timestep.

Interpolations to satisfy a no-slip boundary condition on the immersed boundary

In this immersed boundary method three different interpolations are used. These are drawn schematically in figure 2. The first of these interpolations, a trilinear interpolation, is drawn in figure 2(a). Note that the cell drawn here (the large cube) is not a gridcell, but a cell where at each corner a velocity in a certain direction is defined. Because a staggered grid is used, these cells are different for each velocity component. The point indicated by the grey triangle is the point inside the wall where the velocity is calculated. The black circle indicates the point at the wall where the no slip boundary condition is enforced. It is the point on the wall closest to the grey triangle. Grey squares indicate velocities used in the interpolation. Note that all these velocities must lie outside the boundary for the interpolation to be possible. The velocity at the gray triangle is set in such a way that the interpolated velocity at the black circle is equal to zero. This is done using a normal trilinear interpolation.

In some cases one or more of the points used in the trilinear interpolation lie inside the wall, making a different kind of interpolation necessary. An example of this is drawn in figure 2(b). In this figure, the front face of the cube is suitable for a bilinear interpolation, as only one vertex of this face lies inside the wall. At the point inside the wall, again indicated by a gray triangle, the velocity will be calculated in order to enforce a no-slip boundary condition at the black circle. Used in the interpolation are the velocities at vertices indicated by a grey square. The face is also drawn schematically in figure 3(a). Here the velocity U_1 is calculated using the velocities U_2, U_3 and U_4 to make the velocity at point P equal to zero using the following formula:

$$U_1 = -\frac{U_4(z_2 - z)(r_2 - r) + U_3(z - z_1)(r_2 - r) + U_2(z - z_1)(r - r_1)}{(z_2 - z)(r - r_1)} \tag{7}$$

The point G is a ghostpoint, which lies just as far from the wall as the point (z_1, r_2). At this point the velocity is equal to $-U_1$. The relevance of this ghostpoint will be made clear in the coming subsection.

If a bilinear interpolation is not possible either, it is neces-

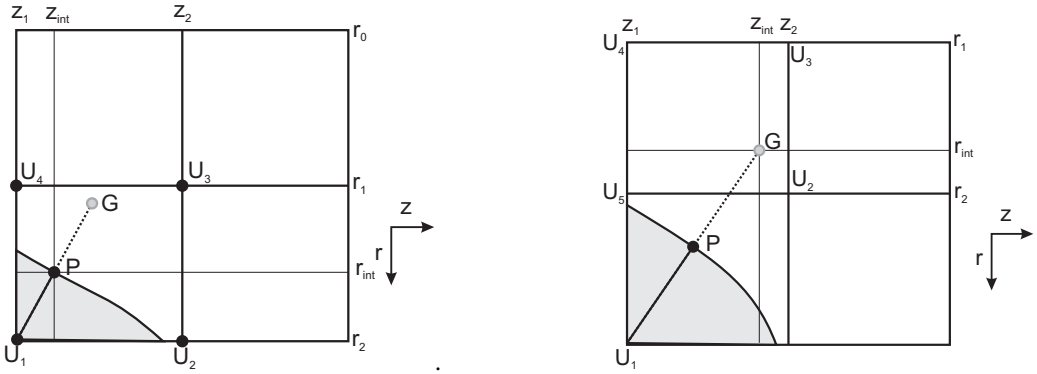

(a) Trilinear interpolation

(b) Bilinear interpolation

FIGURE 3. DIFFERENT TYPES OF INTERPOLATION

sary to use a linear interpolation. Such an occurrence is displayed in figure 2(c). Here the velocity on the point indicated by the gray triangle is calculated using only one other velocity: that indicated by the square. This kind of interpolation was used as an example in the previous subsection and is drawn in figure 1(a). After the predictor step, the velocity inside the wall is given by equation 5.

Now all the basic interpolations used in the implementation of the immersed boundary method are given. However, as Kim et al. [1] showed, these interpolations can lead to numerical instabilities. The problem is shown in figure 1(a). If the wall lies very close to the gridnode for the velocity just outside the wall at $r = r_1$, i.e. $h \gg y_A$, the interpolation of the velocity component will yield a very large value of the velocity just inside the wall at $r = r_2$. This will lead to numerical instabilities, especially where turbulent flow is considered. The solution to this problem is given in the next section.

Problems with the interpolations and their solution

In the paper by Kim et al. a solution for the problem with the linear interpolation discussed at the end of the previous section was already stated. It involves using an additional velocity outside the wall at $r = r_0$ in the interpolation. This is displayed in figure 1(b). If $h > y_A$ the velocity inside the wall after the interpolation is thus given by:

$$U_2 = -\frac{(y_B - h)U_1 + (h - y_A)U_0}{y_B - y_A} \tag{8}$$

The interpolation uses a ghostpoint (indicated by a gray dot at r_g). This ghostpoint and the first gridpoint inside the wall lie at equal distances, but on different sides of the wall, i.e.:

$$r_2 - r_w = r_w - r_g \tag{9}$$

The interpolation works by finding the velocity at the ghostpoint using velocities U_0 and U_1, given by $-U_2$ in the figure. The velocity at the wall is just this velocity mirrored in the wall and is therefore equal to U_2.

When turbulent flow is simulated, the influence of large velocities inside the wall becomes larger, and velocities obtained using trilinear and bilinear interpolations might incite numerical instabilities. These occur when the wall lies closer to a velocity point outside the wall then to the velocity point inside the wall (this is drawn in figure 3(b), where the point P lies closer to U_5 than to U_1). A similar solution is found for these interpolations, as described by Tseng and Ferziger [12]. For each point near the wall a ghostpoint is determined, indicated by the points G in figure 3. If the ghostpoint lies in the same cell as the point just inside the wall, like in figure 3(a), the bilinear interpolation given in equation 7 will be carried out. If the ghostpoint lies in another cell, as in figure 3(b), the velocity in the ghostpoint will be determined using the velocities U_2, U_3, U_4 and U_5. If this velocity is found to be U_g, the velocity U_1 inside the wall will be equal to $-U_g$. A similar technique can also be applied to a trilinear interpolation.

In the simulations performed for this paper, the gridcells are elongated and the wall might shift more than one grid spacing in the r-direction while shifting one gridspacing in the z-direction. This is represented in figure 4. The ghostpoints of two velocity-locations inside the wall are also shown. For the velocity U_{w1} the normal bilinear interpolation from equation 7 is possible. However, for U_{w2} a bilinear interpolation like in figure 3(b) requires the velocity U_{w1} to be set at the correct value. Using the method of Kim et al. [1] a linear interpolation would be employed (also displayed in figure 4). The linear and bilinear interpolations suggested in figure 4 to set velocity U_{w2} differ a lot. This leads to irregularities in the interpolations near the wall. As a solution, first all momentum sources not requiring velocities inside the wall for the interpolation (like U_{w1}) are interpolated, next the interpolations which require one velocity inside the wall (like U_{w2})

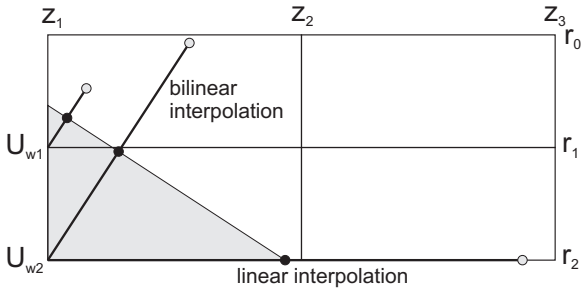

FIGURE 4. PROBLEMS WITH BILINEAR INTERPOLATIONS

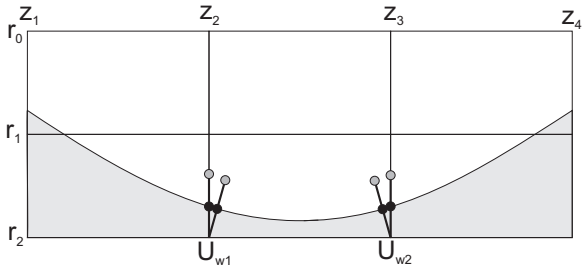

FIGURE 5. INTERPOLATIONS NEAR TROUGH

are performed using the velocities interpolated earlier and so on. This means that for convex boundaries, linear interpolations are no longer required. For concave boundaries however, it is possible that two ghostpoints end up in the same cell. This is shown in figure 5. Here it is not possible to determine the velocities U_{w3} and U_{w4} inside the boundary one by one. In a sinusoidal wall this occurs at points where the diameter reaches its maximum value. It is possible to solve these two equations using a system of two linear equations. However, for a sinusoidal wall at a maximum diameter the function varies little in the radial direction, meaning that at those points the linear and bilinear interpolations are very similar. This is also visible in figure 5. Therefore, instead of using bilinear interpolations, linear interpolations are used at these locations.

Satisfying mass-conservation near the immersed boundary

In the corrector step, the Poisson equation for the pressure-correction ϕ is solved. This is done to satisfy the continuity equation, stating that the divergence of the velocity field of an incompressible fluid should be equal to zero. The Poisson equation reads:

$$\frac{1}{\rho}\nabla_h^2\phi^{n+1} = \frac{1}{\Delta t}\nabla_h \cdot \vec{U}^* \tag{10}$$

where $\vec{U}^*$ is the velocity calculated in the predictor step. The divergence of the velocity in a gridcell is equal to zero if the

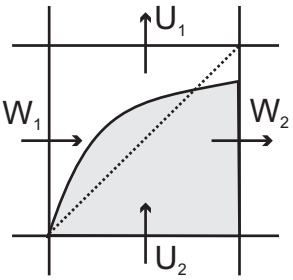

FIGURE 6. EXPLANATION OF A MASS SOURCE

inflow into and the outflow from the gridcell are equal. In the example in figure 6 this is true if:

$$u_1\Delta z - u_2\Delta z + w_1\Delta r - w_2\Delta r = 0 \tag{11}$$

Note that for simplicity the above equation is written in two dimensions and in Cartesian coordinates. In reality 3 dimensional cylindrical coordinates are used. In the figure, the boundary crosses the gridcell and only outside the boundary the mass needs to be conserved. Therefore only the velocities outside the wall will contribute to the divergence. For the current example this means that:

$$w_1\Delta r + u_1\Delta z = 0 \tag{12}$$

Note that each side of a gridcell is treated as either lying completely inside or completely outside the boundary. This is an approximation used to avoid the 'cut cell complication', requiring complex surfaces in three dimensions to be calculated in order to compute the divergence for a given gridcell cut randomly by the boundary. If the calculation of the divergence is not adapted in this way, a large divergence may often be found near the wall due to the velocities just inside the wall. This will cause a large pressure correction near the wall, necessitating large velocity adjustments. After these adjustments the no-slip boundary condition on the immersed boundary will no longer be satisfied, as has been shown by Kim et al. [1], discussing the calculation of the divergence in detail in their paper. Changing the calculation of the divergence is equivalent to introducing a mass source such that:

$$u_1\Delta z - u_2\Delta z + w_1\Delta r - w_2\Delta r + Q\Delta r\Delta z = 0 \tag{13}$$

where in this case the mass source Q is given by:

$$Q\Delta r\Delta z = w_2\Delta r + u_2\Delta z \tag{14}$$

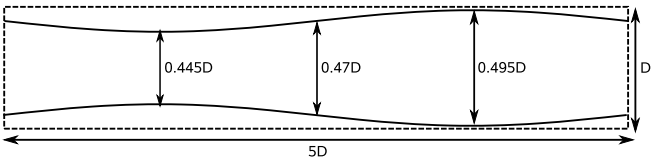

FIGURE 7. DOMAIN FOR VALIDATION USING THE SOLUTION FROM MANTON

to make equations 12 and 13 equal. This mass source will be introduced in the right hand side of the Poisson equation:

$$\frac{1}{\rho}\nabla_h^2\phi^{n+1} = \frac{1}{\Delta t}\left(\nabla_h \cdot \vec{U}^* + Q\right) \tag{15}$$

VALIDATION OF THE IMMERSED BOUNDARY METHOD

In this section the immersed boundary method is validated using results for laminar flow. For the simulations in this section, 64 gridnodes in the radial direction and 128 gridnodes in both the azimuthal and axial directions are used. The grid in the two latter directions is uniform, while arctangent-gridstretching is used in the radial-direction to improve the resolution near the immersed boundary. In all simulations throughout the paper, periodic boundary conditions are implemented in both the angular and axial direction.

Validation using semi-analytical solution

Manton [13] formulated a semi-analytical solution for low Reynolds-number axisymmetric flow in pipes of varying cross-section. This solution is used in the validation of the immersed boundary method. As the expression found by Manton is only valid for pipes with a slowly-varying cross-section, the pipe in figure 7 was selected for the validation. The wall is a sine function with one period in the length of the pipe and an amplitude of about 2.7 % of the average diameter of the pipe. Note that D in this picture is not the average diameter of the pipe, but the diameter of the pipe plus the immersed boundary. The result of the semi-analytical model is given in figure 8, showing the streamlines. Due to the low Reynolds number (Re ≈ 47 based on the average diameter and the bulk velocity) there is no detachment of the flow from the wall. The streamfunction used to plot these streamlines was also used to calculate the radial and axial velocities. They are compared with velocities from the simulations using the immersed boundary method in figure 9. The two different approaches yield similar results, showing that the method currently used works properly for low-Reynolds-numbers and slowly varying pipe cross-sections.

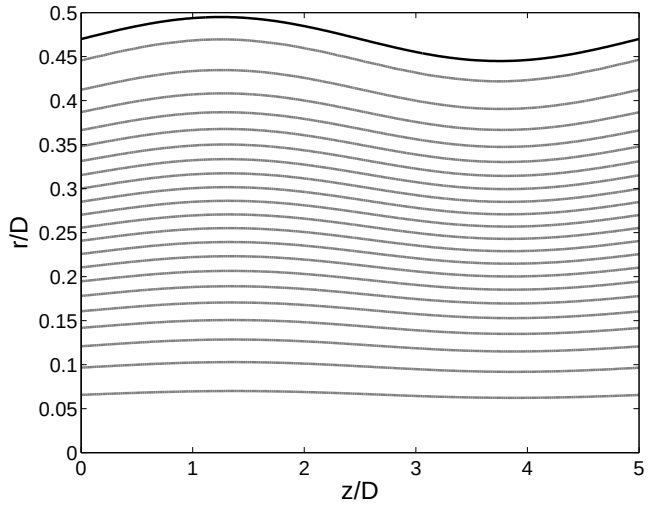

FIGURE 8. STREAMLINES FOR THE SEMI-ANALYTICAL MODEL BY MANTON

Validation using axisymmetric simulation

Next, the method is validated using results for higher Reynolds-numbers (Re $= 300$, again based on the average diameter and the bulk velocity) from axisymmetric simulations by Mahmud et al. [14]. In contrast to the previous validation, the amplitude of the sine function shaping the boundary is much larger (the diameter varies by more than 70%) so that detachment takes place. Because inertia is also more important in these circumstances, it is no longer possible to calculate the flow using a perturbation of Stokes flow in a straight pipe, as was possible in the previous validation. The pipe is drawn schematically in figure 10. The normalised stream function found by Mahmud et al. is drawn in figure 11(a). In figure 11(b) the result obtained using the immersed boundary method is shown. Comparing the two results of figure 11 shows large similarity of the normalised stream function. The only notable difference being the centre of the recirculation area, which lies at a slightly higher axial coordinate in the current simulation. Overall, it seems that the implemented immersed boundary method works properly for laminar flow even with large differences in pipe diameter.

EVALUATION OF THE RESULTS FOR TURBULENT FLOW

In this section the results for turbulent flow are examined. Because no results for turbulent flow in wavy pipes at suitable Reynolds numbers have been found in the literature, validation of the results is not possible. In this section the influence of the gridspacing on the results is considered. These results have been used to determine the required grid resolution. All results in this section are simulated on the computational domain given in figure 12(b). In the coming simulations, 64 gridnodes in the ra-

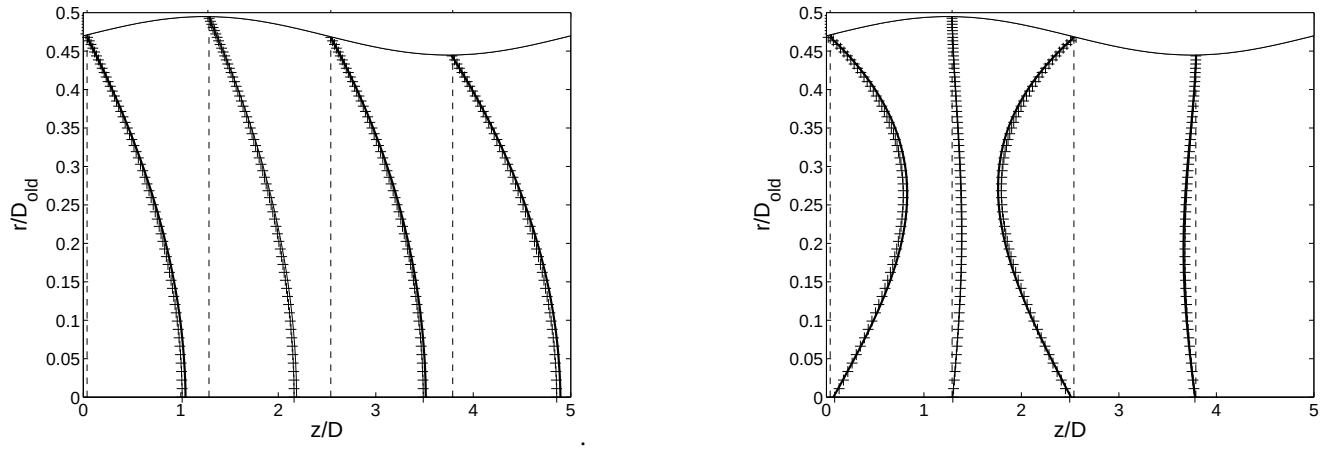

(a) Radial velocity (b) Axial velocity

FIGURE 9. VALIDATION USING SOLUTION BY MANTON

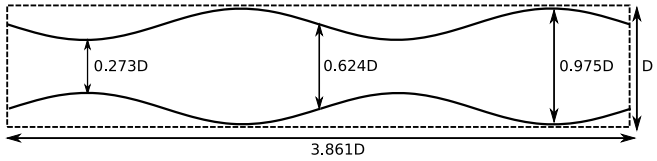

FIGURE 10. DOMAIN FOR VALIDATION USING RESULTS FROM MAHMUD ET AL.

dial direction and 128 gridnodes in the azimuthal direction are used, with grid-stretching in the radial direction. The amount of gridnodes in the axial direction is varied.

The results are all made dimensionless using u_∇, as given by:

$$u_\nabla = \sqrt{-\frac{1}{4\rho} D \frac{\partial p}{\partial z}} \tag{16}$$

where $\frac{\partial p}{\partial z}$ is the average pressure gradient in the pipe and ρ is the density of the fluid. This means that the dimensionless velocity and wall-shear are represented by:

$$U^* = \frac{U}{u_\nabla} \text{ and } \tau^* = \frac{\tau}{\rho u_\nabla^2} \tag{17}$$

These are called outer-units, denoted by a $*$ superscript. The density of the fluid is chosen equal to one. The simulations where all performed at a wall-Reynolds number of 360. The wall Reynolds-number is defined as:

$$Re_\tau = \frac{u_\nabla D}{\nu} \tag{18}$$

where D is the total diameter of the computational pipe, consisting of the pipe itself and the immersed boundary. This is indicated in figure 12. For convenience the $*$-sign will be dropped in the coming sections, however, all quantities given are in outer units.

In the simulations of the laminar flow from the previous section, 128 gridnodes where used in the axial direction. However, when using the same amount of gridnodes for turbulent flow, oscillations appear. To show this, the average radial velocity along the line drawn in figure 12(b) is shown in figure 13. The oscillations are clearly visible when a grid-resolution of only 128 points is used. When the resolution is doubled, the oscillations are almost completely gone. Increasing the resolution to 360 gridpoints in the axial direction does not change the outcome of the simulation significantly, making it plausible that this gridresolution is sufficiently large to yield accurate results. This is the grid-resolution used in the results section. The oscillations are caused by a very large change in velocity within one gridspacing at the immersed boundary. The wavelength of the oscillations is equal to two gridspacings. Increasing the resolution decreases the difference in velocity within one gridspacing, reducing the size of the oscillations. To show how the number of gridnodes affects quantities averaged over the entire pipe, in figure 14 the average axial velocity and the average velocity fluctuations in all directions are drawn, for 128, 256 and 360 gridnodes in the axial direction. Clearly, the results are almost identical for the three

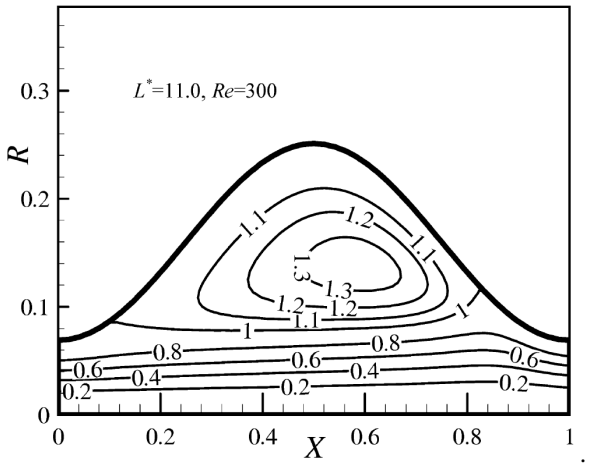

(a) Streamlines by Mahmud

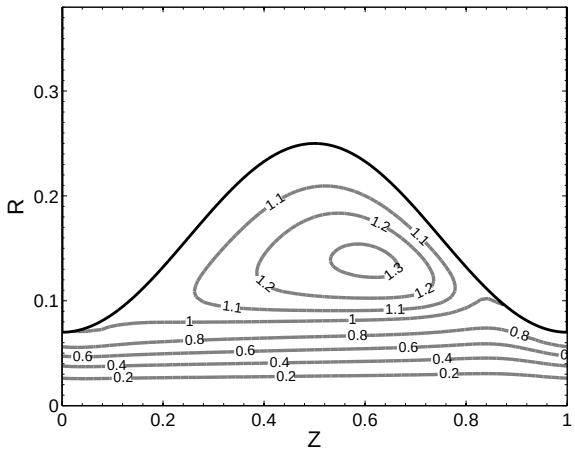

(b) Streamlines using current IBM

FIGURE 11. VALIDATION USING RESULTS BY MAHMUD ET AL. VALUES ON THE AXIS ARE SCALED USING THE WAVELENGTH OF THE SINE FUNCTION SHAPING THE BOUNDARY

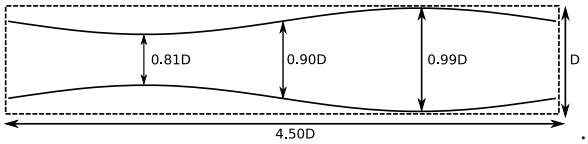

(a) Computational domain with one period of the sine function.

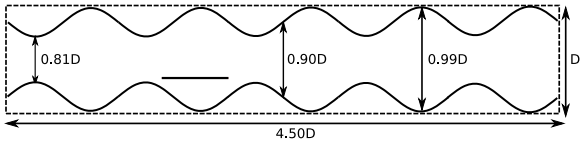

(b) Computational domain with five periods of the sine function.

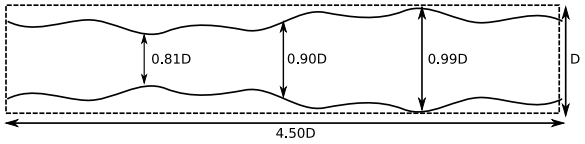

(c) Computational domain with a superposition of one and five periods of the sine function.

FIGURE 12. DIFFERENT WALL TOPOGRAPHIES USED IN THE SIMULATIONS

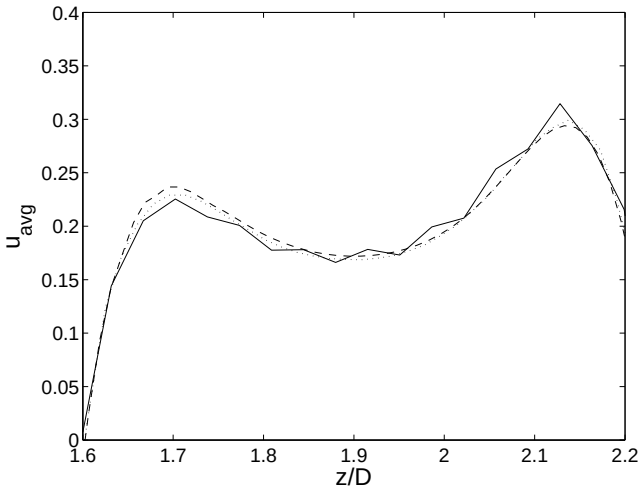

FIGURE 13. AVERAGE RADIAL VELOCITY ALONG THE SMALL LINE DRAWN IN FIGURE 12(b). TOTAL NUMBER OF GRIDPOINTS IN THE Z-DIRECTION: SOLID LINE: 128 GRIDCELLS, DOTTED LINE: 256 GRIDCELLS, DASHED LINE: 360 GRIDCELLS

different resolutions. This means that when only these average quantities are needed, it is sufficient to use 128 grid-points in the axial direction. When more information about the flowfield is required, the resolution must be increased to get a sufficiently accurate result.

RESULTS

In this section the results of the simulations of turbulent flow using the immersed boundary method are given. First, three different wall topographies varying in the axial direction are considered. Subsequently a wall geometry varying in the circumferential direction is discussed.

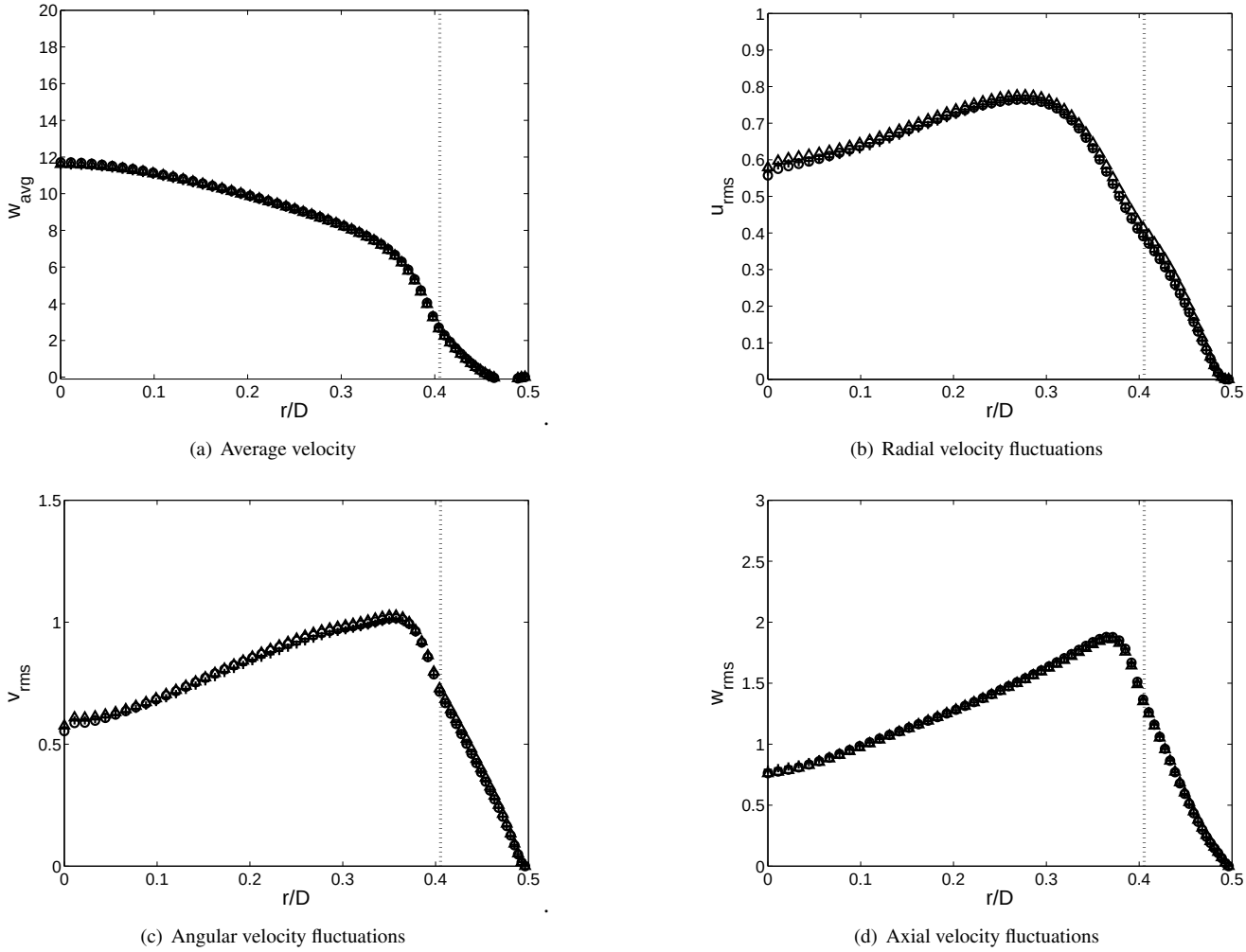

(a) Average velocity

(b) Radial velocity fluctuations

(c) Angular velocity fluctuations

(d) Axial velocity fluctuations

FIGURE 14. STATISTICAL RESULTS FOR SEVERAL GRID RESOLUTIONS. TRIANGLES: 128 GRIDPOINTS, CIRCLES: 256 GRIDPOINTS, PLUS-SIGNS: 360 GRIDPOINTS

Wall geometries varying in the axial direction

The three different wall topographies varying in the streamwise direction are shown in figure 12. In the first domain the wall consists of a sine-function with one period in the entire length of the pipe. This means that the topography does not resemble true roughness, as the wall is only slightly curved. Due to this small curvature the average streamlines, as drawn in figure 15, follow the wall as there is no recirculation zone. The average streamlines resemble the result of Manton [13], given in figure 8. A notable difference is the smaller spacing between the streamlines near the wall in the turbulent flow. This occurs where the flow is squeezed because the pipe diameter decreases. When looking at the results for the instantaneous streamlines in figure 16, the difference with laminar flow is much clearer, because the influence of turbulent velocity fluctuations on these streamlines becomes visible. Note that some streamlines penetrate the wall, indicating that the no-slip boundary condition is not exactly satisfied at the location where the streamline crosses the wall. The interpolations discussed earlier only make the velocity equal to zero in one point on the wall in every gridcell. If the streamline reaches the wall at a different location, the velocity might be slightly larger than zero and the streamline passes through the wall. This is a disadvantage of the crude linear interpolations near the immersed boundary. Because only one cross-section of the pipe for a certain azimuthal coordinate is shown, the divergence is not necessarily equal to zero, causing some streamlines to begin or end suddenly.

The second simulation is of a pipe with a wall topography consisting of a sine function with 5 periods in the length of the pipe, as drawn in figure 12(b). The average streamlines in the rz-plane are drawn in figure 17. The streamlines no longer follow the wall, but recirculation area's appear between the protrusions

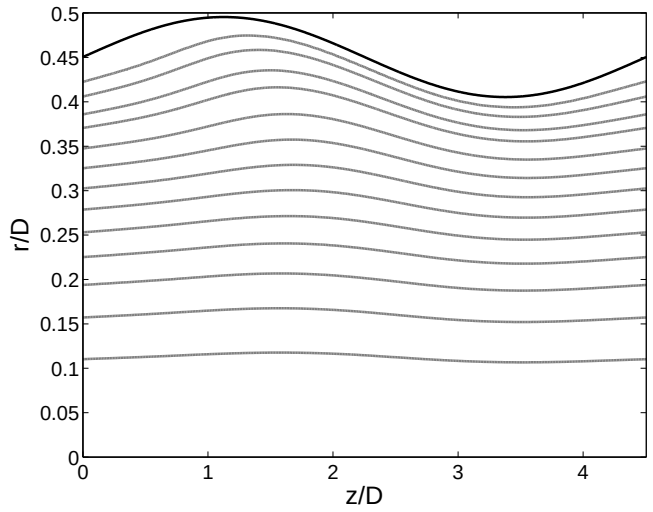

FIGURE 15. AVERAGE STREAMLINES FOR ONE PERIOD

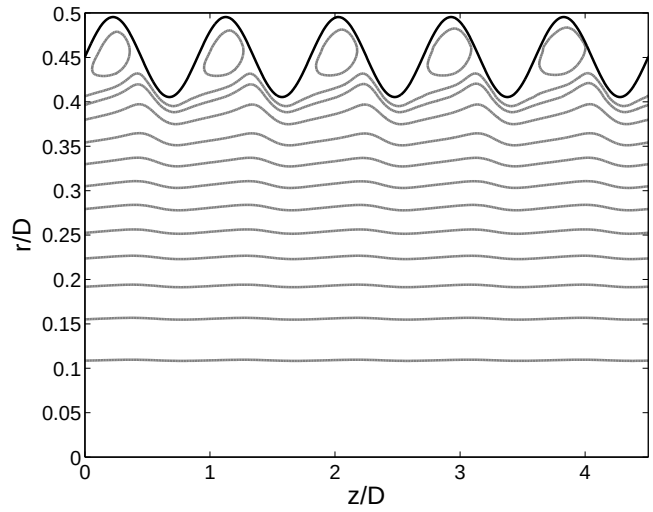

FIGURE 17. AVERAGE STREAMLINES FOR FIVE PERIODS

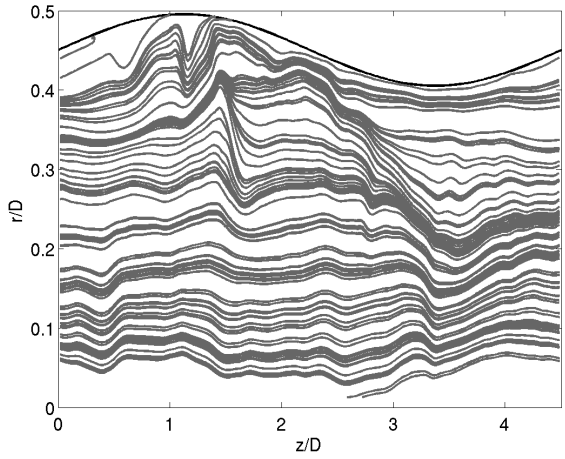

FIGURE 16. INSTANTANEOUS STREAMLINES FOR ONE PERIOD

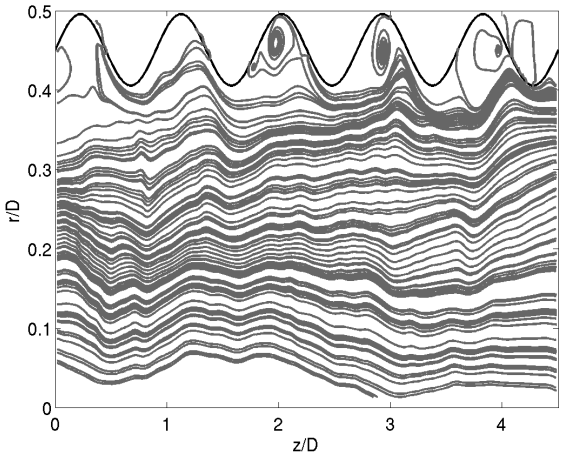

FIGURE 18. INSTANTANEOUS STREAMLINES FOR FIVE PERIODS

in the wall topography. The result resembles the streamlines by Mahmud [14], where the diameter also varied significantly over relatively short distances. The flow detaches from the wall when the period of the sine-function decreases or the amplitude increases. In figure 18 the instantaneous streamlines are plotted.

In the third simulation, the wall topography consists of a superposition of the two sine functions used before: a sine-function with one period in the length of the pipe and one with five periods within this distance. The amplitude of both sine functions is half the amplitude used in the previous two cases, obtaining equal differences in pipe diameter in each simulation. A schematic of this third pipe is given in figure 12(c). The average streamlines in this domain are drawn in figure 19. Note that the result contains some recirculation areas, e.g. at $z = 0.3$, but elsewhere the pipe diameter increases, yet no recirculation area is present. This occurs at $z = 1.1$ where the pipe diameter is largest. For completeness, a snapshot of the instantaneous streamlines can be found in figure 20.

The effect of the wall topography on the flow statistics is depicted in figure 21, where various quantities averaged over the angular and axial directions are shown as a function of the radial coordinate. The three wall geometries given in figure 12 along with a straight pipe with a diameter of $0.90D$ are featured in the graphs. The average velocity, plotted in figure 21(a) is largest for the straight pipe. The different curved wall topographies increase the drag of the wall on the fluid. Note that a higher number of

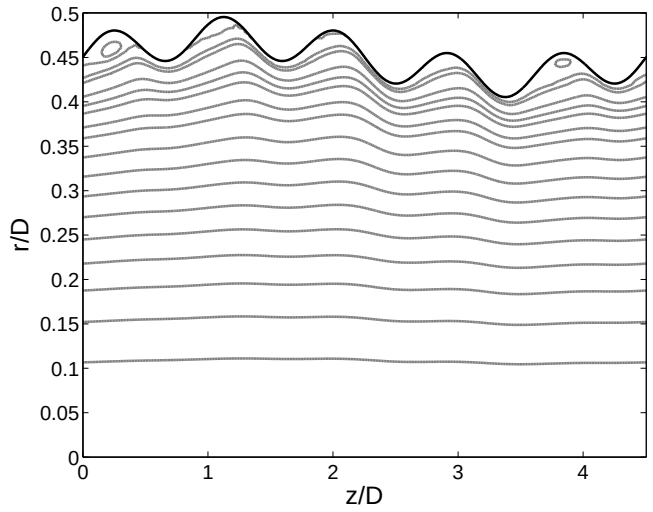

FIGURE 19. AVERAGE STREAMLINES FOR SUPERPOSITION

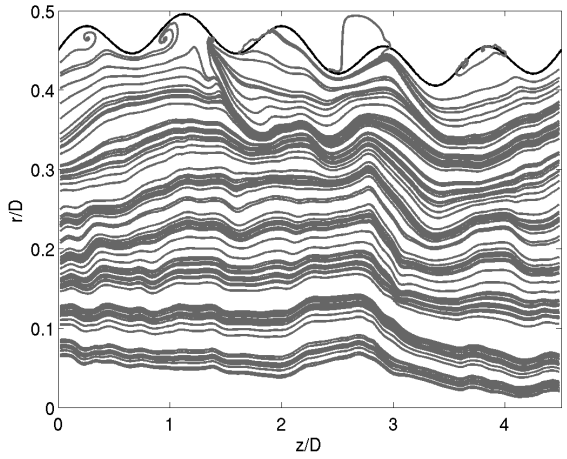

FIGURE 20. INSTANTANEOUS STREAMLINES FOR SUPERPOSITION

periods of the sine function leads to a larger drag. The superposition of the two sine functions yields a result close to that of a single period sine. The streamlines, showing few recirculation areas in the superposition, also show a similar behaviour for the superposition and the one period case.

In figure 21(b) the root-mean-square (rms) fluctuations of the radial velocity are displayed. Note that all fluctuations mentioned in the paper are rms fluctuations. The immersed boundary is confined to the interval between $r = 0.405D$ (indicated by the dotted line in the figures) and $r = 0.495D$. When $r \leq 0.405D$, the radial velocity fluctuations are very similar for the three roughness topographies. Although the magnitude of these fluctuations is slightly different in the outer layer, the qualitative behaviour is the same. This also holds for the rms fluctuations in the axial direction. This is a clear argument for the hypothesis that the flow in the outer layer remains largely unaffected by the roughness. In the inner layer, just outside the roughness, the axial velocity fluctuations in pipes with curved walls differ significantly from fluctuations in the axial direction in a straight pipe. This is not true for the velocity fluctuations in the other directions. This is consistent with results previously obtained for rough walls, e.g. by Flack et al. [15].

In a smooth pipe, the velocity and its rms fluctuations do not vary as a function of the axial coordinate. This is different for pipes with a z-dependant wall topography. In figure 22 the axial velocity and the axial velocity fluctuations are drawn at different z-positions along the pipe. Note that the rms fluctuations are only averaged in the azimuthal direction in this figure. For one period, the average velocity shown in figure 22(a) is positive everywhere. This is also shown by the streamlines in figure 15, where recirculation is absent. Negative velocities do occur when the wall topography consists of five periods: where the diameter is largest the velocity near the wall is negative, which appears as a recirculation area in the streamline plot (figure 17). The velocity fluctuations in the one period results (figure 22(b)) show that their magnitude is larger when the pipe diverges than when it converges. The largest turbulence intensity occurs where the diameter is largest. As seen in figure 21(d), axial velocity fluctuations in the inner layer are larger in the pipe with a one-period wall geometry than in the other pipes.

In the superposition, elements of both its components are present. The average velocity (figure 22(e)) is very close to zero at $z = 1.1$, where the diameter is largest. This explains the lack of streamlines at this location in figure 19. The three other velocity profiles drawn in this figure look much like their counterparts in the five diameter case. Considering the velocity fluctuations, the influence of the one period sine is clear: where this sine is diverging the fluctuations are larger than where it is converging.

In figure 24 the average wall shear for the different roughness topographies is plotted. The calculation of the shear is illustrated in figure 23. The shear can not be calculated inside the wall, because the velocities inside the wall that are not bordering the boundary directly (like at the cross in figure 23) do not have a physical value. Therefore the velocity is obtained using a trilinear interpolation at a distance δ, equal to 0.5 grid-diagonals, from the wall and once more at a distance $\delta + \varepsilon$ from the wall. Because the shear stress is always directed parallel to the wall, the velocity is decomposed into three orthogonal directions, one perpendicular to the wall, one parallel to the wall in the rz-plane (seen in figure 23) and one parallel to the wall in the $r\theta$-plane. In the figure the time-averaged wall shear stress in the rz-plane is given (the average wall shear in the $r\theta$-plane is equal to zero). The velocity parallel to the wall is obtained using the following relation:

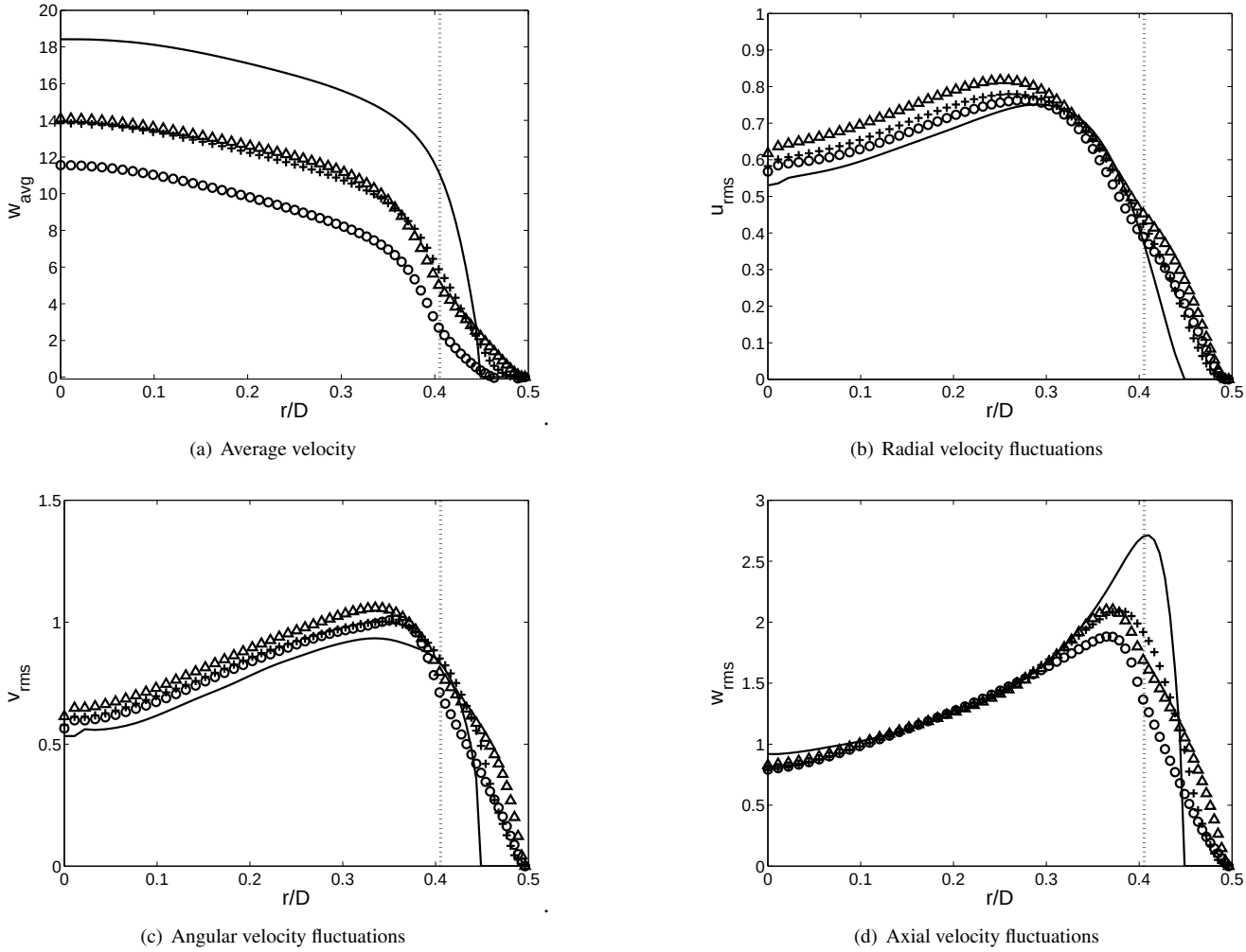

(a) Average velocity

(b) Radial velocity fluctuations

(c) Angular velocity fluctuations

(d) Axial velocity fluctuations

FIGURE 21. RESULTS FOR THE THREE DIFFERENT WALL TOPOGRAPHIES IN FIGURE 12 AND FOR A STRAIGHT PIPE. LINE: STRAIGHT PIPE, TRIANGLES: ONE PERIOD, CIRCLES: FIVE PERIODS, PLUSSES: SUPERPOSITION OF ONE AND FIVE PERIODS THE DOTTED LINE INDICATES THE TOP OF THE WALL TOPOGRAPHY

$$U_{w1} = u_{w1}\sin\phi + w_{w1}\cos\phi \tag{19}$$

where ϕ is the angle between the wall and the horizontal at the location where the shear is calculated. U_{w1} is the velocity parallel to the wall in the rz-plane. In a similar way U_{w2} can be found. The shear stress in this plane is now calculated as follows:

$$\tau_{w,\theta z} = \mu \frac{\partial \overrightarrow{U}}{\partial \hat{n}} \cdot \hat{r} \approx \mu \frac{U_{w2} - U_{w1}}{\varepsilon} \tag{20}$$

where $\hat{n}$ is the unit normal of the wall and $\hat{r}$ the unit normal along the shear component. Figure 24 shows the time-averaged wall shear stress for the three simulations. The average wall shear stress for the one period wall is higher than for the five period wall, while at the five period wall more momentum is lost due to pressure exerted on the wall. This happens when the fluid flows against the boundary where the pipe diameter decreases. At these points there is a large gradient in the velocity component perpendicular to the wall resulting in a pressure force exerted on the wall. The streamline plot (figure 17) shows that just before the pipe reaches its minimal diameter the streamlines quickly change direction, indicating a significant force exerted on the wall. When the wall topography consists of a sine function with only one period, the flow follows the boundary and there are no abrupt changes in the direction of the average streamlines. This indicates that no large pressure forces are exerted on the wall and a larger fraction of the momentum loss is due to shear. The superposition yields a result that looks like a superposition of the two previous results: the five periods are clearly visible in

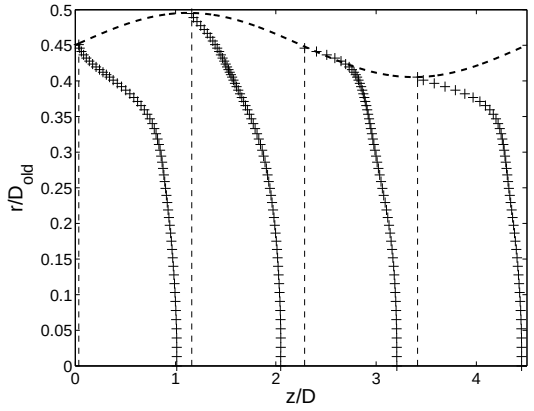

(a) Average velocity on several axial locations along the pipe for one period

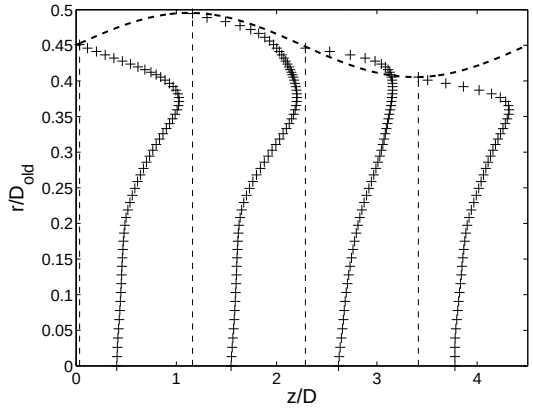

(b) Average fluctuations in the axial velocity on several axial locations along the pipe for one period

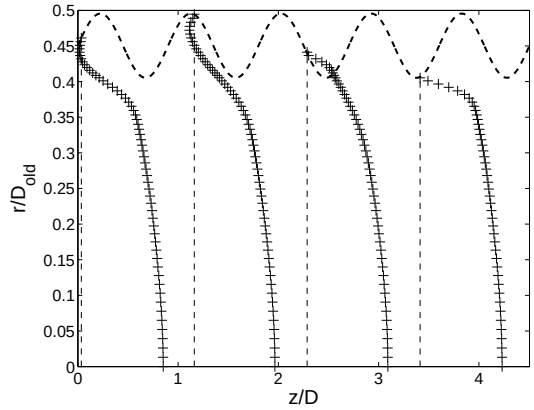

(c) Average velocity on several axial locations along the pipe for five periods

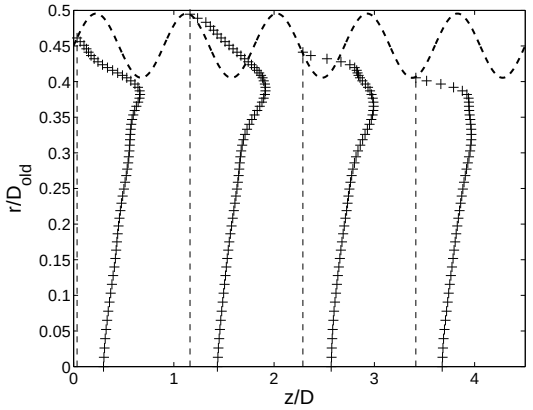

(d) Average fluctuations in the axial velocity on several axial locations along the pipe for five periods

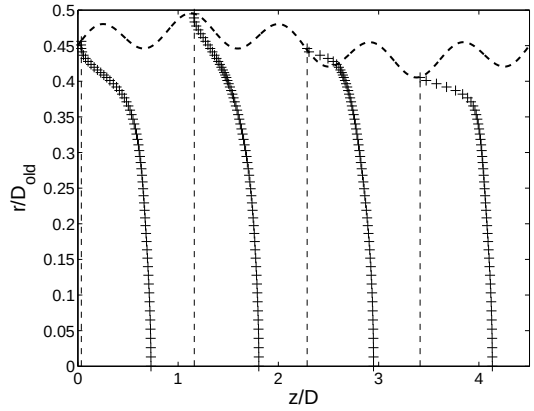

(e) Average velocity on several axial locations along the pipe for the superposition

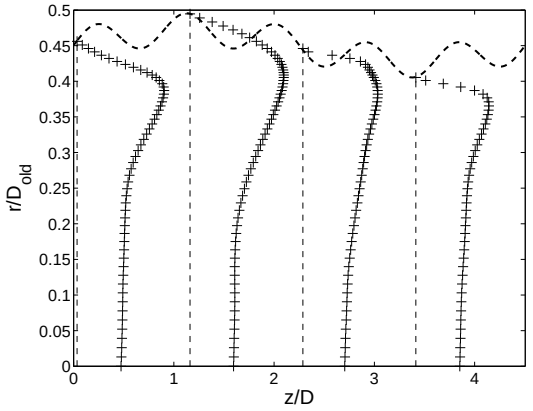

(f) Average fluctuations in the axial velocity on several axial locations along the pipe for the superposition

FIGURE 22. RESULTS FOR THE AVERAGE VELOCITY AND THE VELOCITY FLUCTUATIONS FOR THE THREE SIMULATED CASES FROM FIGURE 12 AT SEVERAL LOCATIONS ALONG THE PIPE

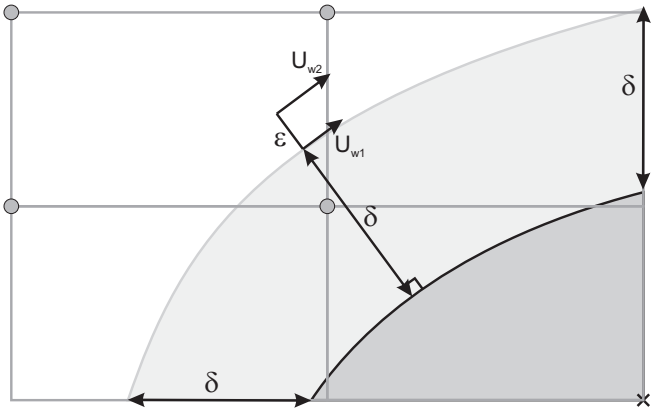

FIGURE 23. THE SHEAR IS FOUND USING VELOCITIES AT DISTANCES δ AND $\delta+\varepsilon$ FROM THE IMMERSED BOUNDARY

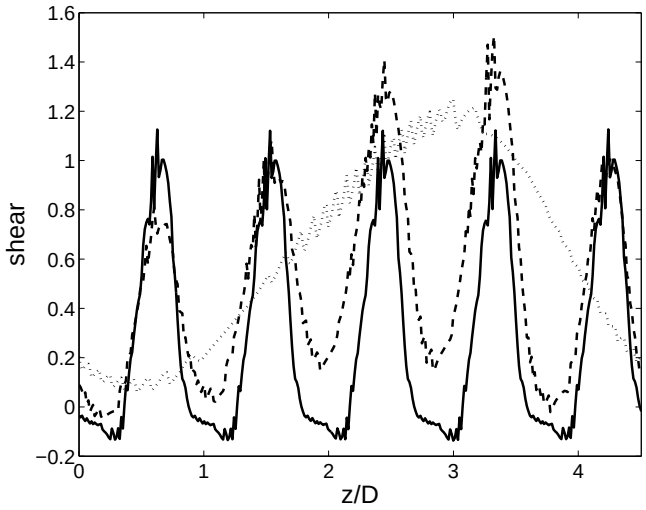

FIGURE 24. AVERAGE SHEAR AT THE WALL FOR ONE PERIOD (DOTTED LINE), FIVE PERIODS (LINE) AND THE SUPERPOSITION (DASHED LINE)

the result, but they are imposed upon a one-period function. Note that the amplitude of the five period component of the wall shear stress becomes larger when the wall lies closer to the centre of the pipe (at $z = 3.3$, where the one period sine is near its minimum). In all results of the wall-shear oscillations are present. Very close to the wall the influence of the crude interpolations is large, yielding these oscillations in the velocity field.

In figure 25 the sum of the shear stresses in the rz-plane and the viscous term ($\overline{u'w'} + \nu\frac{\partial w}{\partial r}$) is drawn for the three wall geometries. In a straight pipe, the result is a straight line. If the pipe diameter is equal to D, the result at the pipe wall is equal to unity, whilst being equal to zero at the centre of the pipe. For the three cases drawn in the figure, the curves are almost straight outside the wall region ($r < 0.405$). The most notable deviation is for the one period case: here the flow does not seem to behave like a normal pipe flow over a rough boundary, but more like a flow in a pipe with varying diameter, yielding a different result near the boundary. The superposition yields a very straight line, indicating that the resultant flow is much like pipe flow over a rough boundary. Inside the roughness (at $r > 0.405D$), the result is no longer given by a straight line. In this region the situation is so different from normal pipe flow, that no constructive comparison can be made.

In figure 26 the contourplot of the magnitude of the instantaneous shear stress is drawn for the one period wall geometry. Superimposed on top of this contour are the streamlines of this shear stress, which indicate the flow near the wall. In this figure the wall was projected upon a flat plane. The darker areas indicate a larger shear stress. At the beginning of the pipe, the diameter increases and the shear stress is small, some streamlines ending on places where the shear stress is equal to zero. Because the shear in the z and θ directions is of the same order of magnitude, the streamlines are curved. When the diameter decreases, the shear in the z-direction becomes much larger and the streamlines will follow a streaky pattern, mostly in the z-direction. This picture is consistent with figure 22(a), where the velocity gradient near the wall is small when the diameter is large and vice versa.

For the superposition, a similar plot was made (figure 27). At the beginning of the pipe, where the one period sine is causing the wall to diverge and the five period-sine has a maximum, the shear is also very small. Around $z = 0.3$ many streamlines end on a position where the shear stress is equal to zero. To a somewhat lesser extend, this also happens one fifth of the pipe further downstream, where the higher frequency sine function has its second maximum. After this point the low frequency sine starts converging, and the shear in the z-direction becomes larger, leading to a streaky pattern of the streamlines. Note that the streamlines tend to cluster more than in the previous case.

Wall geometry varying in the circumferential direction

Using the immersed boundary method, many different wall geometries can be created. As an example of this, in figure 28 the streamlines are given in a cross-section of a pipe with a wall geometry varying in the θ-direction. These variations of the boundary in the azimuthal direction are called ribblets. In the z-direction the cross-section is constant. The statistics for this pipe are given in figure 29 where they are compared to a straight pipe.

The average velocity fluctuations confirm the hypothesis that the flow in the centre of the pipe is little affected by roughness. Due to the ribblets, eddies have more difficulty reaching the wall of the pipe and as a result the velocity fluctuations near the wall are smaller than for the straight pipe. This leads to a decrease of the average wall shear. However, because the surface area of

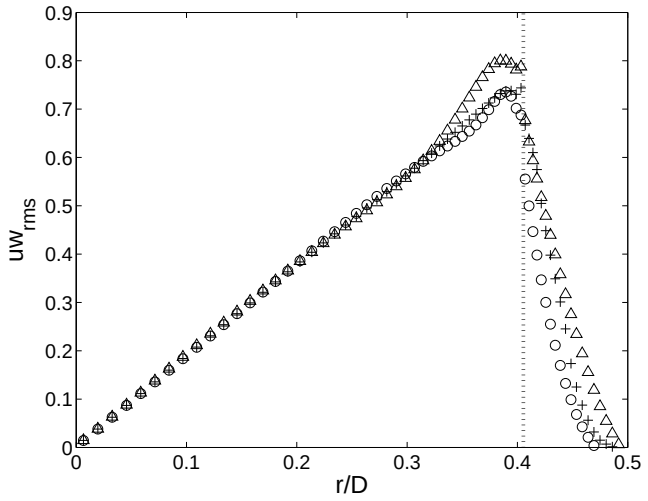

FIGURE 25. VALUES FOR $\overline{u'w'} + \nu \frac{\partial w}{\partial r}$ TRIANGLES: ONE PERIOD, CIRCLES: FIVE PERIODS, PLUSSES: SUPERPOSITION

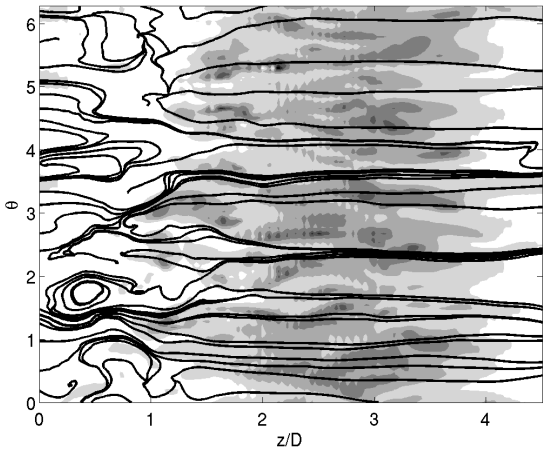

FIGURE 26. CONTOURPLOT OF THE MAGNITUDE OF THE INSTANTANEOUS SHEAR-STRESS ALONG WITH STREAMLINES FOR SUPERPOSITION. DARKER COLOURS INDICATE A LARGER SHEAR STRESS

the wall is larger when ribblets are present, the total wall shear is still slightly larger than for a normal pipe resulting in a slightly lower average velocity.

To illustrate the difference in drag of the several roughness topographies considered in this paper, the Darcy-Weisbach friction factor ($4f$) of each of the wall geometries is given in the table below. The friction factor is calculated using the following

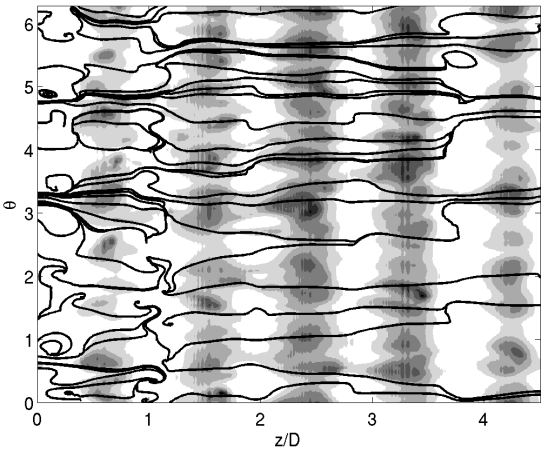

FIGURE 27. CONTOURPLOT OF THE MAGNITUDE OF THE INSTANTANEOUS SHEAR-STRESS ALONG WITH STREAMLINES FOR ONE PERIOD. DARKER COLOURS INDICATE A LARGER SHEAR STRESS

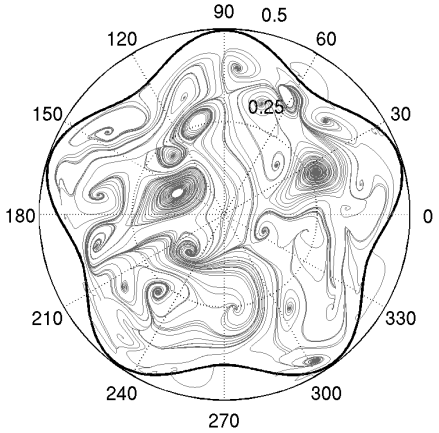

FIGURE 28. INSTANTANEOUS STREAMLINES FOR WALLS VARYING IN THE AZIMUTHAL DIRECTION

equation determined using a balance of forces in the pipe:

$$4f\frac{\rho u^2}{2} = -D\overline{\nabla p} \tag{21}$$

As a comparison, the friction factor calculated using the Colebrook equation [16] is also given in table 1.

CONCLUSION

An immersed boundary method, based on the paper by Kim et al. [1] is developed to implement a varying wall topography into an existing DNS code for pipe flow. This method is validated

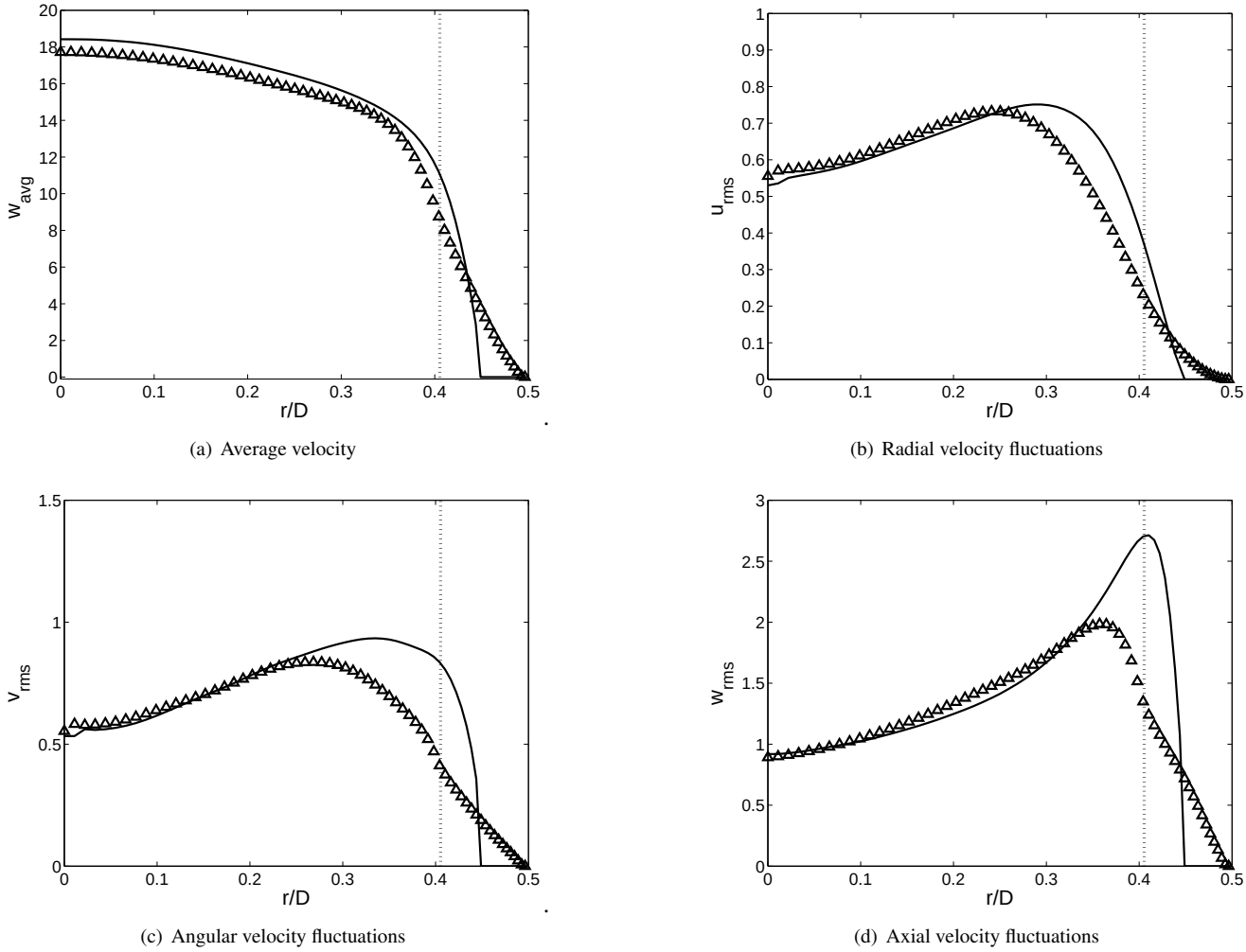

(a) Average velocity

(b) Radial velocity fluctuations

(c) Angular velocity fluctuations

(d) Axial velocity fluctuations

FIGURE 29. RESULTS OF THE WALL VARYING IN THETA. LINE: RESULTS FOR A SMOOTH WALL, TRIANGLES: RESULTS FOR WALL VARYING IN THE AZIMUTHAL DIRECTION.

for laminar flow using results from a semi-analytical solution and numerical simulations. From this validation it is concluded that the method yields accurate results for laminar flow even when the diameter of the pipe varies dramatically. Four simulations for turbulent flow where performed, each with a different wall geometry. For three of these geometries, the wall varied in the axial direction, in the fourth geometry, it varied in the azimuthal direction. The results presented for turbulent flow are consistent with the expected physical behaviour. They confirm the hypothesis that flow in the outer layer is largely unaffected by the wall topography. Some inaccuracies in the flowfield occur near the wall, yielding oscillations in the inner layer when the grid resolution is to small. When higher grid resolutions are used these oscillations are confined very close to the wall, but show up in the plots of the shear stress. However, these disadvantages of the immersed boundary method are minor. The big advantages such as the absence of complicated body conformal grids and the possibility to use fast solvers far outweigh these shortcomings. For future research, this code can be used to simulate roughness geometries varying in both the axial and the azimuthal directions.

REFERENCES

[1] Kim, J., Kim, D., and Choi, H., 2001. "An immersed-boundary finite-volume method for simulations iof flow in complex geometries". *Journal of Computational Physics, **171***, pp. 132–150.

[2] Moody, L. F. "Friction factors for pipe flow". In Transactions of the A.S.M.E.

[3] Bhaganagar, K., and Hsu, T., 2008. "Direct numerical simulations of flow over two-dimentional and three-dimentional ripples and implication to sediment transport".

wall geometry	$4f$
smooth wall	0.036
one period in axial direction	0.078
five periods in axial direction	0.15
superposition in axial direction	0.079
five periods in azimuthal direction	0.043
roughness from Colebrook equation	0.15

TABLE 1. FRICTION FACTORS OF THE DIFFERENT WALL GEOMETRIES. FOR COMPARISON THE FRICTION FACTOR FROM THE COLEBROOK EQUATION IS GIVEN

Coastal Engeneering, ***56***, pp. 320–331.

[4] Jiménez, J., 2004. "Turbulent flows over rough walls". *Annular Review of Fluid Mechanics,* ***36***, pp. 173–196.

[5] Bhaganagar, K., Kim, J., and Coleman, G., 2004. "Effect of roughness on wall-bounded turbulence". *Flow, Turbulence and Combustion,* ***72***, pp. 463–492.

[6] Townsend, A. A., 1976. *The Structure of Turbulent Shear Flow*. Cambridge University Press.

[7] Krogstad, P.-A., and Antonia, R., 1994. "Structure of turbulent boundary layers on smooth and rough walls". *Journal of Fluid Mechanics,* ***277***, pp. 1–21.

[8] Krogstad, P.-A., Antonia, R., and Browne, L., 1992. "Comparison between rough- and smooth-wall turbulent boundary layers". *Journal of Fluid Mechanics,* ***245***, pp. 599–617.

[9] Eggels, J., 1994. "Direct and large eddy simulation of turbulent flow in a cylindrical pipe geometry". PhD thesis, Delft University of Technology.

[10] Goldstein, D., Handler, R., and Sirovich, L., 1993. "Modeling a no-slip flow boundary with an external force field". *Journal of Computational Physics,* ***105***, pp. 354–366.

[11] Prosperetti, A., and Tryggvason, G., eds., 2007. *Computational Methods for Multiphase Flow*, 1 ed. Cambridge University Press.

[12] Tseng, Y., and Ferziger, J., 2003. "A ghost-cell immersed boundary method for flow in complex geometry". *Journal of Computational Physics,* ***192***, pp. 593–623.

[13] Manton, M., 1971. "Low reynolds number flow in slowly varying axisymmetric tubes". *Journal of Fluid Mechanics,* ***49***(3), pp. 451–459.

[14] Mahmud, S., Islam, A. S., and Feroz, C., 2003. "Flow and heat transfer characteristics inside a wavy tube". *Heat and mass transfer,* ***39***, pp. 387–393.

[15] Flack, K. A., Schultz, M. P., and Shapiro, T. A., 2005. "Experimental support for townsends reynolds number similarity hypothesis on rough walls". *Physics of fluids,* ***17***(3).

[16] Colebrook, C., 1939. "Turbulent flow in pipes, with particular reference to the transition region between the smooth and rough pipe laws". *Journal of the ICE,* ***17***(3), pp. 133–156.